Research Paper

Implantation of Iron(III) in porphyrinic metal organic frameworks for highly improved photocatalytic performance

Li Shi[a,b], Liuqing Yang[b], Huabin Zhang[b], Kun Chang[b], Guixia Zhao[b], Tetsuya Kako[b], Jinhua Ye[a,b,c,d,*]

[a] Graduate School of Chemical Sciences and Engineering, Hokkaido University, Sapporo, 060-0814, Japan
[b] International Center for Materials Nanoarchitectonics (WPI-MANA), National Institute for Materials Science (NIMS), 1-1 Namiki, Tsukuba, Ibaraki, 305-0044, Japan
[c] TU-NIMS Joint Research Center, School of Materials Science and Engineering, Tianjin University, 92 Weijin Road, Nankai District, Tianjin, 300072, PR China
[d] Collaborative Innovation Center of Chemical Science and Engineering, Tianjin, 300072, PR China

ABSTRACT

Herein a simple approach is proposed to greatly improve the photocatalytic performance of a porphyrinic metal organic framework (PCN-224) by implantation of coordinatively unsaturated Fe(III) sites into the porphyrin unit. Taking the photooxidation of isopropanol (IPA) as a model reaction, the newly developed Fe@PCN-224 exhibits significantly enhanced photocatalytic activity, which is equivalent to an 8.9-fold improvement in acetone evolution rate and 9.3-fold enhancements in CO_2 generation rate compared with the PCN-224. Mechanism investigation reveals that the presence of Fe(III) sites in the PCN-224 can not only greatly boost the electron–hole separation efficiency, but also effectively convert the in-situ photogenerated inactive H_2O_2 into reactive oxygen-related radicals via Fenton reactions to participate in the photocatalytic IPA oxidation. The enhanced photocatalytic activity for IPA oxidation is also observed over another Fe(III) implanted porphyrinic metal organic framework (Fe@PCN-222), suggesting the generality of this strategy.

1. Introduction

The design and construction of efficient photocatalysts for maximizing the solar-light energy utilization remains crucial in the field of photocatalysis [1–4]. To meet the challenges, various photocatalysts have been developed, among which metal organic frameworks (MOFs) based maerials have drawn considerable and increasing attention [5–10]. MOFs are class of crystalline materials that are constructed from well-defined molecular building blocks and metal or metal-cluster connecting nodes. Recently, many MOFs materials have shown semiconductor-like characters in photocatalysis, and have achieved potential applications in all kinds of photocatalytic areas, such as H_2/O_2 evolution from water splitting [11–13], organic pollutant photo-decomposition [14,15], inorganic hazardous substances photo-reduction [16–18], CO_2 reduction [19–23], and so on. However, the photocatalytic efficiency of MOFs based photocatalysts is still very low and far from satisfaction for the practical needs, largely due to the low efficiency in light harvesting and the fast recombination of the photogenerated electron–hole pairs. In this context, great efforts have been devoted to improve the photocatalytic efficiency of MOFs based photocatalysts over past few years and most of the reported strategies were

limited to a narrow range by either modulation of their organic linkers (e.g., tethering the ligand with one or two additional amine groups) or incorporation with dye/semiconductor catalysts for enlarged visible light absorption, better charge separation, and efficient reactant activation [24–31]. Developing novel strategies to dramatically boost the photocatalytic efficiency of MOFs based photocatalysts is desperately needed.

The modification of transition metal ions, such as Fe(III), on photocatalysts has been proved as an efficient way to realize high photocatalytic performance [32,33]. Because of the relative low redox potentials of $Fe^{3+/2+}$ compared with the conduction band positions of photocatalysts, the photogenerated electrons from photocatalysts can be easily scavenged by the modified Fe(III) ions, inducing the efficient separation of electron-hole pairs, which should be beneficial for the photocatalytic reactions [33]. Fe(III) ions were also be used as a reactant in light induced heterogeneous Fenton-like photocatalytic process to produce abundant and active oxygen-related species ($\cdot OH$ and $\cdot O_2^-$), which play an essential role in promoting the photocatalytic activities for oxidation of organic molecular [34,35]. The generally accepted free-radical-chain mechanism of Fenton reaction between Fe^{3+}/Fe^{2+} pair and H_2O_2 is shown below [34]:

$$Fe^{2+} + H_2O_2 \rightarrow Fe^{3+} + \cdot OH + OH^-$$

$$Fe^{3+} + H_2O_2 \rightarrow Fe^{2+} + \cdot O_2H + H^+$$
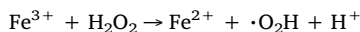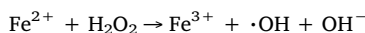
In most cases, however, extra H_2O_2 must be added into the reaction system as a reactant to initiate those Fenton-like reactions, which is not cost-effective [35–37]. Very recently, it has been demonstrated that a Fenton reaction could be constructed on Fe(III) modified alkalinized-C_3N_4 photocatalyst even without adding extra H_2O_2, in which the light energy was used as power, alkalinized-C_3N_4 photocatalyst acted as an in situ and robust H_2O_2 generator, and the modified Fe^{3+} acted as a trigger of H_2O_2 conversion to produce considerably abundant oxygen-related radicals [38]. To initiate this Fenton reaction, an indispensable issue that must be mentioned is the capability of photocatalysts to photogenerate H_2O_2. It has been reported that porphyrins and their derivatives owned the ability to effectively photogenerate H_2O_2 [39,40]. We can reason that the photogeneration of H_2O_2 might be realized *via* integration of porphyrins unites into MOFs structure. Bearing these in mind and motivated by the fact that the unique structural properties of porphyrins could provide the effective co-ordination sites to anchor individual metal ions [41,42], we can reasonably expect that the Fe(III) could be rationally modified on porphyrinic MOFs based photocatalysts, which would result in much improved separation efficiency of electron-hole pairs, as well as initiate the Fenton-like reactions to produce active oxygen-related species, and finally improve the photocatalytic activities.

In this work, we employed a very stable porphyrinic MOF, PCN-224, which integrate the Zr_6 clusters and porphyrin based molecular units into 3D network, as a visible light active photocatalyst for isopropanol (IPA) oxidation. Coordinatively unsaturated Fe(III) ions are implanted into porphyrin unit and generate a new hybrid structure Fe@PCN-224. The introduction of Fe(III) ions in PCN-224 can not only improve the separation efficiency of photogenerated electron-hole pairs, but also construct a Fenton reaction to convert the *in situ* photogenerated H_2O_2 into active oxygen-related radicals ($\cdot OH$ and $\cdot O_2^-$) during the photocatalytic reaction. As a direct result, the newly developed Fe@PCN-224 exhibits significantly enhanced photocatalytic oxidation of IPA, which is equivalent to an 8.9-fold improvement in acetone evolution rate and 9.3-fold enhancements in CO_2 generation rate compared with the PCN-224. Furthermore, apart from PCN-224, such Fe(III) implantation-enhanced photocatalytic IPA oxidation performance could also be observed over another porphyrinic MOF, PCN-222, suggesting the generality of this strategy.

2. Experimental section

2.1. Preparation of photocatalysts

In the synthesis of PCN-224, 120 mg $ZrOCl_2·8H_2O$ (Wako Co.,) was added to *N, N*-dimethylformamide (DMF, 50 ml) and stirred for thirty minutes. After that, 25 mg tetrakis(4-carboxyphenyl)-porphyrin (TCI, Tokyo Chemical Industry Co.,) was added to the solution. After ten minutes further stirring, acetic acid (12.5 ml) was added to the solution. The solution was heated at 338 K for three days in the autoclave. The generated precipitate was collected by centrifugation, washed repeatedly by methanol and dried under vacuum at 80 °C. Fe@PCN-224 was prepared as follows: 100 mg of PCN-224 and 200 mg of $FeCl_3$ were mixed together into 20 ml DMF solution and stirred for 30 min at room temperature. After that the solution was heated at 120 °C with stirring for 12 h, and the generated precipitate was collected by centrifugation, washed repeatedly by methanol and dried. The weight percentage of the Fe in PCN-224 was measured by inductively coupled plasma (ICP)-elemental analysis, which was 4.1 wt.%. Fe & PCN-224 was prepared as follows: 100 mg of PCN-224, 13.5 mg $FeCl_3$ (4.1 wt.% Fe in Fe & PCN-224) and 3 ml ethanol were ground together in a mortar under room temperature. After the evaporation of ethanol, the powder sample was

collected and then dried under 60 °C for 6 h.

PCN-222 was prepared according to the following procedure. $ZrOCl_2·8H_2O$ (75 mg) was added to DMF (20 ml) and stirred for thirty minutes. Following stirring, tetrakis(4-carboxyphenyl)-porphyrin (13 mg) was added to the solution. After a further ten minutes of stirring, formic acid (14 ml) was added to the solution. The solution was heated at 130 °C for three days in the autoclave, and then the generated precipitate was collected by centrifugation, washed repeatedly by methanol and dried under vacuum at 80 °C. Fe@PCN-222 was prepared similarly to Fe@PCN-224 except that PCN-224 was replaced by PCN-222.

NH_2-MIL-125 was synthesized by adding 2-amino benzenedi-carboxylic acid (6 mmol) and titanium isopropoxide (3 mmol) into a solution containing DMF (25 ml) and methanol (25 ml). The mixture was stirred at ambient temperature for 30 min, transferred to Teflon lined stainless steel autoclave, and heated 16 h at 423 K. After the reaction, the product of the synthesis was extracted by centrifugation, and washed with methanol. The obtained yellow solid was dried under vacuum overnight. NH_2-UiO-66 was prepared as follows: $ZrCl_4$ (0.240 g) and 2-amino benzenedicarboxylic acid (0.186 g) were added into DMF (60 ml) solution at room temperature. The mixed solution was stirred at room temperature for 30 min and transferred to Teflon lined stainless steel autoclave and heated at 120 °C for 48 h. After hydrothermal treatment, the resultant suspension was filtered, washed with DMF and methanol several times, and dried under vacuum overnight. For the synthesis of MIL–88 B (Fe), benzenedicarboxylic acid (3 mmol, 0.498 g) and $FeCl_3·6H_2O$ (3 mmol, 0.811 g) were dissolved in DMF (50 ml). After vigorously stirred for 10 min, this solution was placed in a sealed vessel and heated by microwave at 400 W for 15 min at 150 °C. After cooling to room temperature, the resulting particles were isolated by centrifugation, washed with ethanol and deionized water several times, and then dried at 343 K under vacuum overnight. g-C_3N_4 was prepared by heating melamine to 550 °C for 4 h under air condition in a crucible.

2.2. Characterization

The crystal structure of the samples were characterized by powder XRD (SmartLab). The UV–vis spectra of the samples were measured on a UV–vis spectrophotometer (SHIMADZU UV-2600) and $BaSO_4$ was used as the reflectance standard reference. The morphology analysis of the as-prepared samples was conducted on a scanning electron microscope (SEM, S4800, Hitachi Co., Japan). TEM, HAADF-STEM, and elemetal mapping images were taken on a transmission electron microscope (TEM, 2100F, JEOL Co., Japan). Nitrogen adsorption–desorption isotherms and BET surface areas were recorded using a Quantachrome Autosorb-iQ Automated Gas Sorption System at 77 K, and the pore size distributions were analyzed by density functional theory (DFT) model. Before nitrogen adsorption–desorption measurement, the samples were treated under vacuum at 150 °C for 12 h. The PL spectra of samples were recorded on the powder samples by using JASCO FP-6500 spectrofluorometer. The PL lifetime measurements were performed on a compact fluorescence lifetime spectrometer (Quantaurus-Tau, C11367, HAMAMATSU). the chemical state of the samples were analyzed by X-ray photoelectron spectroscopy (XPS, PHI Quantera SXM, ULVAC-PHI Inc., Japan). The chemical structure of the samples was studied by FTIR spectra (Thermoscientific Nicolet 4700). The ESR measurements were carried out with JEOL JES-FA-200 at room temperature.

2.3. Photoelectrochemical measurement

The photoanodes are prepared as follows. Clean indium tin oxide (ITO) glass was first obtained by sequentially washing with acetone, distilled water, and ethanol in an ultrasonic cleaner for 30 min. Then, 2 mg photocatalyst was well dispersed in 1 ml ethanol containing 10 μl nafion and stayed in an ultrasonic cleaner for 30 min. Subsequently, all
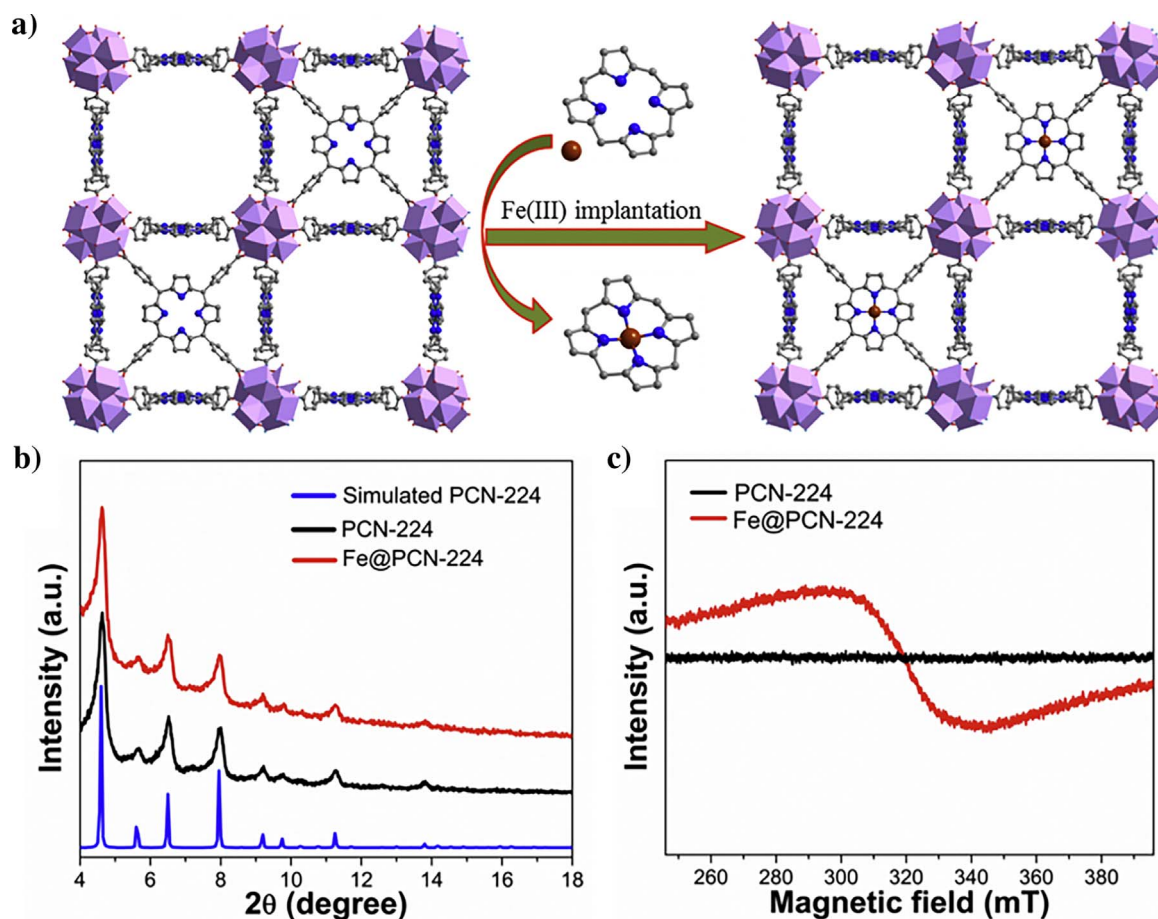
Fig. 1. (a) View of the 3D network of PCN-224 featuring highly porous framework as well as the implantation of Fe(III) sites into the PCN-224 framework; (b) XRD patterns of PCN-224 and Fe@PCN-224; (c) ESR spectra of PCN-224 and Fe@PCN-224.

the above suspension was deposited dropwise by using a pipette onto the surface of an ITO glass with exposed $1 \times 1 \text{ cm}^2$ area uniformly. After drying overnight in an oven, the electrodes were sintered at 100 °C in N_2 for 2 h to improve adhesion. The loading mass is about 2 mg/cm^2. The boundary of ITO glass was protected using transparent tape.

The photoelectrochemical measurements were carried out in an electrochemical station (ALS/CH model 650A, Japan). The as-prepared PCN-224 and Fe@PCN-224 photoanodes ($1.0 \times 1.0 \text{ cm}^2$) were used as a working electrode, a Pt foil was used as a counter electrode, a Ag/AgCl electrode was used as the reference electrode, and a 0.5 M Na_2SO_4 solution was used as the electrolyte. A 500 W Xe lamp with a UV-cutoff filter ($\lambda > 400$ nm) was used as the visible light source. The photocurrent was measured at -0.5 V bias voltage *versus* Ag/AgCl. The Mott-Schottky plots were obtained in the dark at 1000 and 500 Hz.

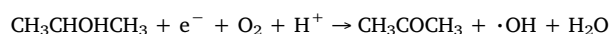### 2.4. The measurement of H_2O_2

The measurement of H_2O_2 was conducted by using the colorimetric DPD method. The DPD method is based on the oxidation of *N,N*-diethyl-*p*-phenylenediamine (DPD) catalyzed with horsedish peroxides (POD) by H_2O_2. Briefly, 0.1 g of DPD was dissolved in 10 ml 0.05 M H_2SO_4, denoted as solution A. 10 mg of peroxidase (POD) was dissolved in 10 ml water, denoted as solution B. 10 ml of 0.1 M Na_2HPO_4 solution and 90 ml of 0.1 M NaH_2PO_4 solution were mixed together to obtain solution C. Then 54 ml deionized water, 6 ml solution C, 24 μl methanol, 100 μl solution A and 100 μl solution B were mixed together to obtain solution D. The *in-situ* generated H_2O_2 during the photocatalytic IPA oxidation was measured as follows: the 20 mg photocatalyst sample
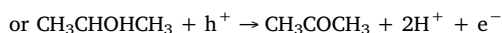
powder was irradiated under visible-light for 5 min in the reaction cell with gaseous IPA and air addition, and then was dispersed into solution D, 3 ml filtrates was used to measure the generated H_2O_2, which was monitored by the absorption of the solution at 551 nm and determined with UV–vis spectrophotometer. The time-dependent H_2O_2 generation was measured in a similar above procedure expect that the irradiation time was set as 10, 15, 20, 25 min, respectively.
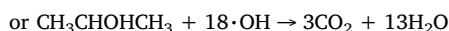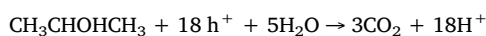
2.5. Photocatalytic experiments

A 300 W Xe arc lamp (focus through a 45×45 mm shutter window) equipped with a UV light cutoff filter ($\lambda > 400$ nm) and a cooling water filter was employed as the light source. 0.05 g of the sample was evenly spread over a dish with an area of 8.5 cm^2 in a 500 ml borosilicate glass vessel. The experimental facility can be seen from Fig. S7. Then the vessel was pretreated by artificial air [V(O$_2$):V (N$_2$) = 1:4] for 5 min to remove the gaseous impurities. After the sample was sealed in the vessel, a certain amount of gaseous isopropanol (IPA) was injected into the vessel. Before exposed to the visible light irradiation, the reaction cell was kept in dark to ensure an adsorption–desorption equilibrium. The generated concentration of acetone and CO_2 was measured by using a gas chromatograph (GC-2014, Shimadzu Corp., Japan) equipped with FID detectors and methanizer. The photocatalytic IPA oxidation undergoes two kinds of typical reaction processes as below [38]:

(1) One-photon reaction:

$$CH_3CHOHCH_3 + e^- + O_2 + H^+ \rightarrow CH_3COCH_3 + \cdot OH + H_2O$$

$$\text{or } CH_3CHOHCH_3 + \cdot OH \rightarrow CH_3COCH_3 + H_2O + H^+ + e^-$$

or $CH_3CHOHCH_3 + h^+ \rightarrow CH_3COCH_3 + 2H^+ + e^-$

(2) Multiphoton reaction:

$CH_3CHOHCH_3 + 18\,h^+ + 5H_2O \rightarrow 3CO_2 + 18H^+$

or $CH_3CHOHCH_3 + 18\cdot OH \rightarrow 3CO_2 + 13H_2O$

3. Results and discussions

3.1. Synthesis and characterization of photocatalysts

Solvothermal treatment of zirconyl chloride octahydrate, tetrakis(4-carboxyphenyl)-porphyrin (H_2TCPP) and acetic acid in DMF solution yielded dark red-colored crystals of PCN-224. PCN-224 crystallizes in space group Im$\bar{3}$m, and its framework consists of Zr_6 clusters linked by the square planar H_2TCPP ligands [43]. Each $Zr_6(OH)_8$ core, in which all of the triangular faces in a Zr_6-octahedron are capped by μ_3-OH groups, is connected to six H_2TCPP ligands (Figs. 1 a, S1). The phase purity of the as-prepared sample was confirmed by X-ray powder diffraction, which is in good agreement with the simulated PCN-224 structure (Fig. 1b). Cationic Fe(III) was incorporated into porphyrin unit (Fig. 1a) and generate a hybrid structure Fe@PCN-224 by post-synthetic reaction between PCN-224 and $FeCl_3$ in DMF solution. The XRD pattern in Fig. 1b shows that the PCN-224 and Fe@PCN-224 exhibit the similar diffraction pattern, indicating that the crystal phase structure is retained after Fe(III) incorporation. The electron spin resonance (ESR) spectrum of Fe@PCN-224 in Fig. 1c displays a strong signal at g value of 1.996, which can be ascribed to the high-spin state Fe(III), confirming the incorporation of Fe(III) into PCN-224 structure [16]. The X-ray Photoelectron Spectroscopy (XPS) spectra were further recorded to determine the chemical state of the Fe species (Fig. 2a). In the Fe 2p core level spectrum, the peak observed at around 711 eV can be assigned to Fe^{3+}, which is consistent with the ESR results illustrated above [38]. The fourier transform infrared (FTIR) spectroscopy is shown in Fig. 2b, compared with H_2TCPP ligand, the asymmetric vibrational absorption intensity of C=O and C−OH groups greatly decrease after coordination between Zr^{4+} and −COOH groups in PCN-224, indicating that the −COOH groups in H_2TCPP ligands are participated in the coordination with Zr^{4+} [44]. N−H bond absorption is observed in H_2TCPP and PCN-224, which confirms the existence of the uncoordinated nitrogen sites in the PCN-224 [45]. By post-synthetic modification of PCN-224 with Fe(III) ions, it can be observed that there is no N−H bond adsorption in the as-synthesized Fe@PCN-224 (See the magnified FTIR spectra in Fig. 2c). Moreover, an intense symmetric Fe−N stretching at around 1000 cm^{-1} appears for Fe@PCN-224 (Fig. 2d), further reflecting the metalation of porphyrin ring with Fe to form iron porphyrinate [45]. All the above results support the successful incorporation of Fe(III) into the porphyrin unit in PCN-224.

The obtained PCN-224 grows into big cubic crystals, which are distributed in the size of several micrometers, as revealed by scanning electron microscopy (SEM) images (Fig. 3a, b). Incorporation of Fe(III) into PCN-224 would not significantly change its morphology (Fig. 3c, d). Fig. 3e–i show the high-angle annular dark-field scanning TEM (HAADF-STEM) image and the corresponding elemental mapping analysis of Fe@PCN-224. It clearly shows the well-defined spatial distributions of element Fe, N, Zr and O, which confirms that Fe is uniformly incorporated in the PCN-224. The existence of Fe element can also be evidenced by the energy dispersive X-ray spectrometer (EDS) spectrum (Fig. S2). The N_2 adsorption-desorption measurements at 77 K for PCN-224 and Fe@PCN-224 show a type I isotherm (Fig. S3). PCN-224 has the stronger ability for N_2 adsorption with the Brunauer–-Emmett–Teller (BET) surface areas of 2726 $m^2\,g^{-1}$, which is higher than that of Fe@PCN-224 (2360 $m^2\,g^{-1}$). The reason may be ascribed to the introduction of Fe sites, which can slightly diminish the surface area. Fig. S4 shows the pore size distribution of PCN-224 and Fe@PCN-

224. The desirable porous structures and high surface area of PCN-224 and Fe@PCN-224 allow for exposing active sites as much as possible and facilitating the accessibility of target reactants to the active sites, which might be advantageous for photocatalysis.

The incorporation of Fe(III) into PCN-224 would induce the color change from dark red to brown (Fig. 4a, inset). The UV–vis spectra in Fig. 4a indicates that PCN-224 is an excellent photon absorbers from 250 to 700 nm, which allows for promoting the electrons of PCN-224 to an excited state upon visible light irradiation. According to $(\alpha h\nu)^{1/2} = A(h\nu\text{-}Eg)$, where α, ν, A and Eg are absorption coefficient, light frequency, proportionality constant and indirect band gap energy, respectively, the calculated indirect bandgap of the PCN-224 is 1.75 eV (Fig. S5). After the metalation of the porphyrin ring with Fe(III), the Fe@PCN-224 hybrid structure can extend light absorption edge to 1000 nm, which can be ascribed to the fact that the incorporation of Fe(III) in the PCN-224 structure can lower its band gap energy by introducing unoccupied Fe(III) trap levels between the valence band maximum (VBM) and the conduction band minimum (CBM) of PCN-224 [30]. These introduced trap levels allow for excitation of electrons from VBM of PCN-224 to the trap levels when subjected to near-infrared illumination.

In order to elucidate the semiconductor character of PCN-224, Mott−Schottky measurements on PCN-224 photoanode were conducted at frequencies of 500 and 1000 Hz (Fig. 4b). The positive slope of the obtained C^{2-} to potential plot is consistent with that of typical n-type semiconductors, [46] and the derived flat-band potential for PCN-224 is −0.50 V *versus* Ag/AgCl (Fig. 4b). Considering the small difference between the flat-band potential and the lower CB edge for n-type semiconductors, the CBM position of PCN-224 can be roughly estimated to be +0.11 V (*vs*. RHE). With the bandgap energy of PCN-224 estimated to be 1.75 eV from the Tauc plot (Fig. S5), its VBM position is then calculated to be +1.86 V (*vs*. RHE). Moreover, the PCN-224 photoanode produces an obvious photocurrent response to on-off cycles of light illumination with the bias potential applied under visible light irradiation, demonstrating that electron-hole pairs are generated over PCN-224 under visible light irradiation (Fig. S6). These results indicate that PCN-224 should be a suitable candidate for light harvesting and photocatalysis.

3.2. Photocatalytic performance evaluation

IPA as a typical volatile organic compound in industry is a serious pollutant of indoor air [38]. In order to test the photocatalytic activity of PCN-224 and assess the validity of the Fe(III) implantation on improving photocatalytic efficiency, we designed a solid-gas reaction system for photocatalytic IPA oxidation (Fig. S7). It is notable that the IPA photo-oxidation includes both a single-photon route to generate the initial product of acetone and a multiphoton route to yield the complete degradation product of CO_2 (see equations in Experimental section) [38,47]. The clear reaction mechanism and typical intermediate product enable us to evaluate the photocatalytic performance of PCN-224 and Fe@PCN-224. Fig. 5a presents the time-dependent photocatalytic acetone evolution over PCN-224 and Fe@PCN-224, respectively. Since the generation of each acetone molecule from IPA usually requires one hole, while the reaction of IPA to CO_2 is a more complex multiphoton-involved process, it's understandable that the photocatalytic oxidation of IPA to acetone is easier than that to CO_2. As shown in Fig. 5b, the generation rate of acetone is much higher than that of CO_2 for both PCN-224 and Fe@PCN-224, which indicates that one-photon reaction takes the predominance role. The calculated acetone evolution rate of Fe@PCN-224 is 280.7 ppm/h, which delivers over 8.9 folds higher than that of PCN-224 (31.6 ppm/h). Moreover, the CO_2 evolution rate of Fe@PCN-224 is also much higher than PCN-224, further indicating the much higher photocatalytic activity of Fe@PCN-224 compared with PCN-224. This experiment demonstrates the superiority of the Fe(III) incorporation into the PCN-224 for the photocatalytic IPA oxidation.
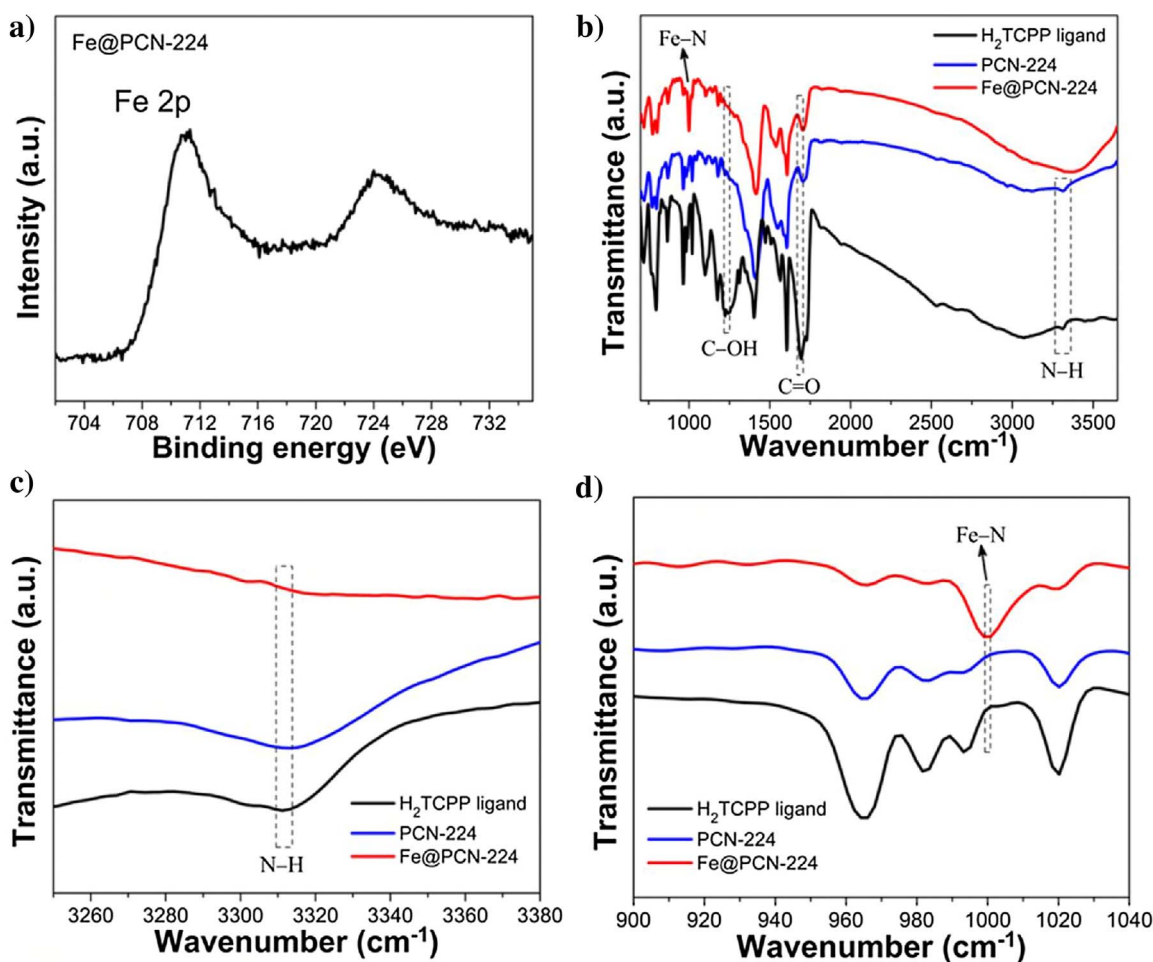
Fig. 2. (a) high resolution Fe XPS spectrum of Fe@PCN-224; (b) FTIR spectra of H₂TCPP ligands, PCN-224 and Fe@PCN-224; (c)-(d) The magnified FTIR spectra of H₂TCPP ligands, PCN-224 and Fe@PCN-224.

Fe@PCN-224 shows much higher photocatalytic activity than Fe coordinated tetrakis(4-carboxyphenyl)-porphyrin (Fe-TCPP), as shown in Fig. S8. Moreover, Fe@PCN-224 also exhibits much higher photocatalytic activity for IPA oxidation than NH₂-MIL-125 (Ti), NH₂-UiO-66 (Zr), MIL–88 B (Fe), g-C₃N₄ and commercial α-Fe₂O₃ under the same reaction conditions (Fig. S9, S10). Moreover, as shown in Table S1, the achieved photocatalytic activity of Fe@PCN-224 for IPA oxidation to acetone is also higher than some reported photocatalysts, which further demonstrates the superiority of Fe@PCN-224 for photooxidation of IPA [48–52].

The stability and reusability of the Fe@PCN-224 photocatalyst were investigated. After the reaction, the Fe@PCN-224 was removed from the reaction system and characterized by FTIR spectra (Fig. S11), XRD pattern (Fig. S12) and morphology analyses (Fig. S13). The results show that the Fe@PCN-224 has strong resistance to chemical structure, crystal structure and morphology changes during the photocatalytic IPA oxidation reaction. The reusability of the photocatalyst was studied by reusing the photocatalyst for four times. As shown in Fig. 5c, the Fe@PCN-224 exhibits fairly good photocatalytic activity stability in the recycling test.

3.3. Photocatalytic mechanism

The above results clearly demonstrate the superiority of Fe(III) implantation in porphyrin MOF for photocatalysis. We are now in a position to understand the mechanisms behind the function of the newly developed structures. To gain insight into the enhancement of photocatalytic activity, we firstly explored the influence of Fe(III)

implantation on the transfer and utilization of the photocarriers (photoexcited electrons and holes) of PCN-224 photocatalyst. Quick recombination of photocarriers is one of the main reasons to limit the photocatalytic activity of a photocatalyst [53]. Fe(III) implantation into PCN-224 can effectively improve the separation efficiency of the photoinduced electron-hole pairs, as reavealed by the photoluminescence (PL) and fluorescence lifetime measurements (Fig. 4c, d). The pronounced PL emission quenching and slightly decreased fluorescence lifetime is due to the fast capture of photogenerated electrons from the CBM of PCN-224 by Fe(III) trap site, which indeedly demonstrated the electron transfer from PCN-224 to Fe(III) trap site, implying the greatly suppressed radiative electron-hole recombination in PCN-224 after Fe (III) implantation. The trapping of photo-generated carriers by trap sites can induce fast fluorescence decay, which is consistent with some reported papers [54,55]. To gain further evidence of electron transfer process, *in-situ* ESR studies were also carried out. As shown in Fig. S14, Fe@PCN-224 in the dark gives a typical ESR signal ascribed to Fe^{3+}. When visible light is irradiated on the above reaction system, the ESR signal is gradually quenched. The decrease of Fe^{3+} ESR signal intensity could be attributed to the trapping of electrons by Fe(III) site in Fe@PCN-224. The electron trasfer in Fe@PCN-224 can effectively improve the separation efficiency of electron-hole pairs. The Fe@PCN-224 also shows improved photoelectochemical performance, as revealed by the enhanced transient photocurrent response (see more details in Fig. S6). The VBM position of PCN-224 is estimated to be +1.86 V (*vs.* RHE), which can reach the oxidation potential of IPA (+0.32 V *vs.* SHE) [56]. Therefore, the photogenerated holes in PCN-224 can oxidize IPA, and the suppressed radiative electron-hole recombination in PCN-224 after
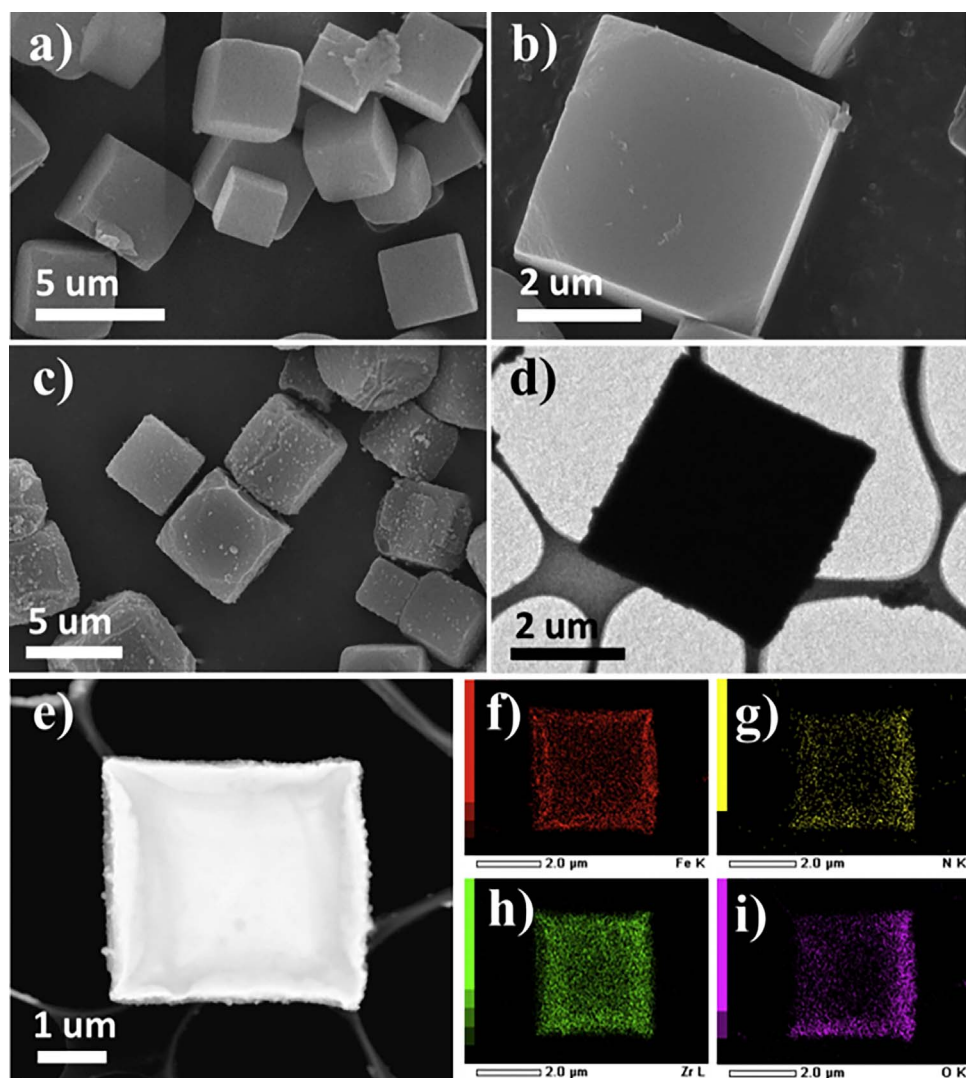
Fig. 3. (a)–(b) SEM images of PCN-224; (c)–(d) SEM and TEM images of Fe@PCN-224, respectively; (e)–(i) HAADF-STEM image and its corresponding elemental mapping images of Fe@PCN-224. (f) Fe, (g) N, (h) Zr, (i) O.

Fe(III) implantation is one of the reasons that the photocatalytic activity is improved for Fe@PCN-224.

In the photocatalytic IPA oxidation process, in addition to the direct hole oxidation, the oxygen-related radicals are considered as highly active species (see equations in Experimental section). To verify if the oxygen-related radicals are participated in the photocatalytic IPA oxidation reactions, the radicals trapping experiments were performed by adding *p*-benzoquinone (pBQ) and coumarin (Cou) as $\cdot O_2{}^-$ and $\cdot OH$ radicals scavenger, respectively, to the photocatalytic reaction system. For the PCN-224 sample, the addition of pBQ and Cou hardly blocks the photocatalytic process, indicating that the oxygen-related radicals did not participate in the photocatalytic IPA oxidation reaction (Fig. S15). However, the pBQ and Cou can obviously suppress the photocatalytic process for the Fe@PCN-224, indicating that $\cdot O_2{}^-$ and $\cdot OH$ radicals join its IPA photooxidation reaction (Fig. S15). The generation of the $\cdot O_2{}^-$ and $\cdot OH$ radicals over Fe@PCN-224 can be evidenced by ESR and 5,5-dimethyl-1-pyrroline-*N*-oxide (DMPO) spin-trapping technique [57]. Fig. 6a, b show the ESR spectra of PCN-224 and Fe@PCN-224 in the presence of DMPO as spin-trapping agent. Obviously, PCN-224 cannot produce $\cdot O_2{}^-$ and $\cdot OH$ radicals, since neither DMPO-$\cdot OH$ signals nor DMPO-$\cdot O_2{}^-$ signals were detected under visible light irradiation. This is largely due to the fact that the potential of the VBM and CBM positions of PCN-224 is located at $+1.86$ V (*vs.* RHE) and $+0.11$ V (*vs.* RHE), respectively, which thermodynamically disfavors for the oxidation of OH$-$ to $\cdot OH$ ($+1.9$ V *vs.* NHE, pH = 7) or reduction of O_2

to $\cdot O_2{}^-$ (-0.33 V *vs.* NHE, pH = 7) [58]. However, the production of $\cdot O_2{}^-$ and $\cdot OH$ was observed over Fe@PCN-224 under visible light, as confirmed by the formation of characteristic peaks of DMPO-$\cdot \cdot OH$ and DMPO-$\cdot \cdot O_2{}^-$ adducts (Fig. 6a, b). In most case, the $\cdot O_2{}^-$ and $\cdot OH$ radicals are generated under Fenton reactions and the H_2O_2 is one of the important reactant [38]. In a photocatalytic process for degradation of gaseous organic compounds, H_2O_2 can be produced *via* photocatalytic reduction of O_2 ($O_2 + 2H^+ + 2e^- \rightarrow H_2O_2$, $+0.695$ V *vs.* SHE) [59]. Since the CBM of PCN-224 has more negative potential, it is believed that this reaction can be achieved in theory. However, convincing experimental results are still necessary to prove the capability of PCN-224 to photogenerate H_2O_2 under visible light irradiation.

To determine the generated H_2O_2 in our photocatalytic process, we designed the experiment as following. The sample powder was irradiated under visible-light for several min with gaseous IPA and air addition, and then was dispersed into an as-prepared solution; the filtrate was used to measure the generated H_2O_2 *via* *N,N*-diethyl-*p*-phenylenediamine (DPD)–horseradish peroxidase (POD) method (See more details in Experimental section) [38]. Fig. 6c shows the time-dependent absorption spectra of the DPD/POD-PCN-224 solution and Fig. S15 shows the time-dependent absorption spectra of the DPD/POD-Fe@PCN-224 solution. The concentration of H_2O_2 can be monitored by the absorption intensity of the solution at 551 nm. Fig. 6d shows the time-dependent concentration evolution of H_2O_2 produced by PCN-224 and Fe@PCN-224, respectively. For PCN-224, the concentration of H_2O_2
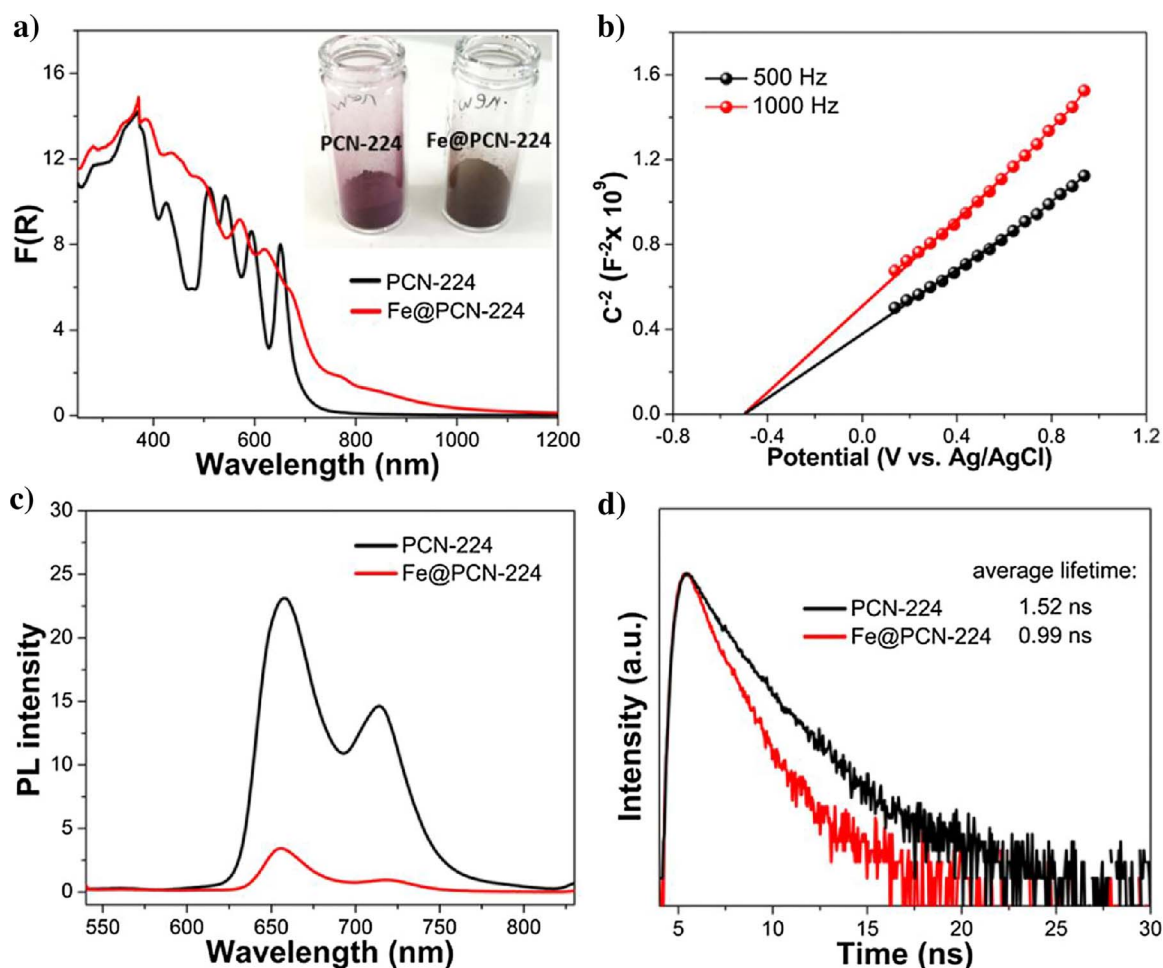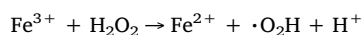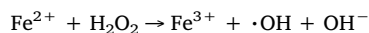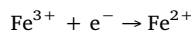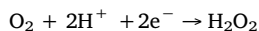
Fig. 4. (a) UV–vis spectra and photograph (inset) of PCN-224 and Fe@PCN-224, respectively; (b) Mott−Schottky plots of PCN-224; (c)-(d) PL spectra and lifetime decay curves of PCN-224 and Fe@PCN-224, respectively.(For interpretation of the references to colour in this figure legend, the reader is referred to the web version of this article.)

increases almost linearly as irradiation time prolongs, indicating that PCN-224 is able to produce H_2O_2 in the photocatalytic reaction system. H_2O_2 was not formed in a control experiment when air was replaced by Ar in the photocatalytic reaction, indicating that H_2O_2 was indeed generated from photocatalytic O_2 reduction by PCN-224. It shows that the evolved H_2O_2 is difficult to be observed over Fe@PCN-224 (Figs. 6 d, S16), which can be reasonably explained that the generated H_2O_2 by PCN-224 quickly reacts with Fe^{2+}/Fe^{3+} pairs, which derives from Fe^{3+} reduced by photoelectron to form $\cdot O_2^-$ and $\cdot OH$ radicals *via* Fenton reactions [38]. The reactions can be described as below [38]:

$$O_2 + 2H^+ + 2e^- \rightarrow H_2O_2$$

$$Fe^{3+} + e^- \rightarrow Fe^{2+}$$

$$Fe^{2+} + H_2O_2 \rightarrow Fe^{3+} + \cdot OH + OH^-$$

$$Fe^{3+} + H_2O_2 \rightarrow Fe^{2+} + \cdot O_2H + H^+$$

On the basis of the above results, a tentative photocatalytic process for gaseous IPA oxidation over the Fe(III)@PCN-224 hybrid structure was proposed in Fig. 6e. Under visible light irradiation, the PCN-224 structure is photoexcited to generate electron–hole pairs, and the separation efficiency can be significantly improved after incorporation of Fe(III) into the structure of PCN-224. The long-lived holes remained in the VBM of PCN-224 can oxidize the IPA to produce acetone and H^+, and a few of photoelectrons in the CBM are consumed to form H_2O_2.
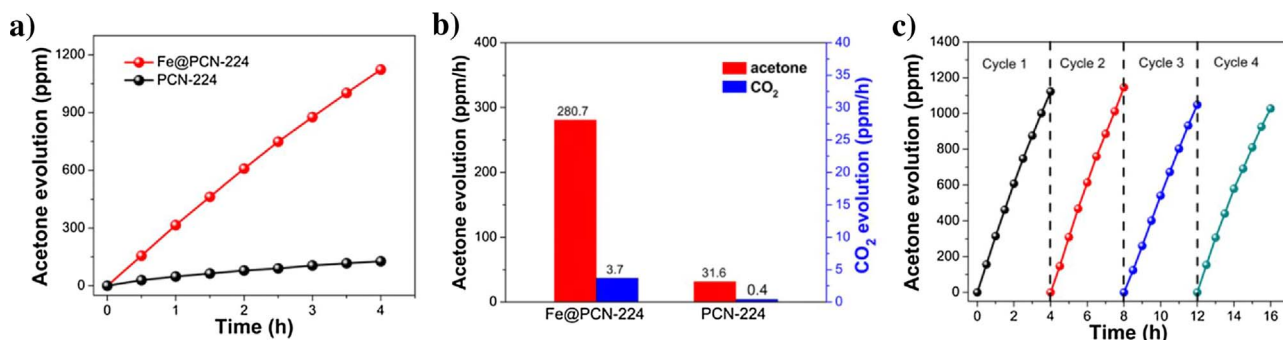

Fig. 5. (a) Time-dependent acetone evolution from photocatalytic IPA oxidation by PCN-224 and Fe@PCN-224; (b) acetone and CO_2 evolution rate comparison between PCN-224 and Fe@PCN-224; (c) photocatalytic acetone evolution stability test on Fe@PCN-224.
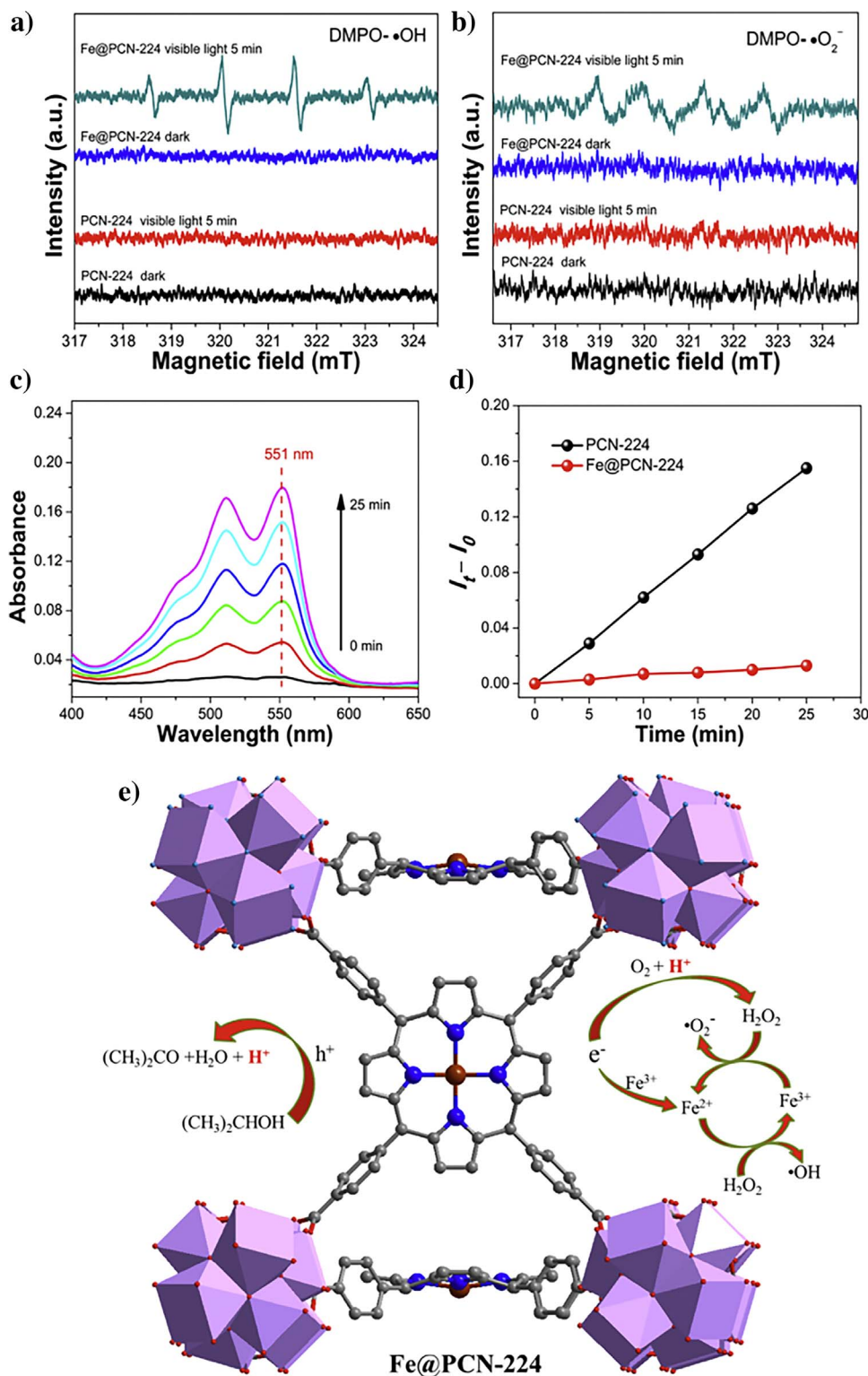
Fig. 6. (a)-(b) ESR signals of DMPO-·OH adducts and DMPO-·O_2^- adducts produced by PCN-224 and Fe@PCN-224 samples, respectively; (c) time-dependent absorption spectra of the DPD/POD-PCN-224 solution; (d) time-dependent concentration evolution of H_2O_2 produced by PCN-224 and Fe@PCN-224, respectively; (e) proposed mechanism of oxygen related radicals generation in photocatalytic systems with Fe@PCN-224.

Simultaneously, a few of electrons may also reduce the incorporated Fe^{3+} to Fe^{2+} ions, and then the formed Fe^{2+}/Fe^{3+} pairs interact with the formed H_2O_2 to generate active ·O_2^- and ·OH radicals through the Fenton reactions, and therefore greatly enhances photoactivity. In order to further demonstrate the superiority of the Fe(III) implantation into the porphyrin unit of PCN-224 for photocatalysis, the Fe(III) loaded at the surface of PCN-224, named as Fe & PCN-224, was prepared through mixing Fe(III) and PCN-224 at room temperature (see experimental section), and its photocatalytic activity for IPA oxidation was also

investigated. The result showed that the photocatalytic activity of Fe@PCN-224 was much higher than Fe & PCN-224 (Fig. S17). It was found that the Fenton reactions could also be constructed on Fe & PCN-224 (Fig. S18). However, its lower efficiency in charge carriers seperation would result in much lower photocatalytic activity compared with Fe@PCN-224 (Fig. S19).

Since the Fe(III) implantation in PCN-224 have a great effect on improving its photocatalytic performance, it is very interesting to investigate the photocatalytic performance of other porphyrinic MOFs

based photocatalysts. PCN-222 was selected because this kind of porphyrinic MOF has been proven to be a stable photocatalyst and contain the H_2TCPP organic linker similar to that in PCN-224 but have different structure [22]. Moreover, Fe(III) implanted Fe@PCN-222 can also be obtained through a post-synthetic modification method. The formation of these MOFs has been confirmed by their XRD patterns (Fig. S20). Those XRD patterns were in good agreement with the simulated PCN-222 structure. The photocatalytic oxidation of IPA was also investigated over PCN-222 and Fe@PCN-222. It is obvious that Fe@PCN-222 shows an greatly improved photocatalytic performance compared to PCN-222 without Fe(III) implantation (Fig. S21). This observation indicated that Fe(III) implantation in porphyrinic MOFs could be a general method to improve the photocatalytic performance for the oxidation of IPA.

4. Conclusion

In summary, we herein propose a novel strategy to boost the photocatalytic efficiency of a porphyrinic MOF photocatalyst (PCN-224) for IPA oxidation *via* post-synthetic implantation of Fe(III). Mechanism study indicates that the implantation of Fe(III) ions in PCN-224 can not only improve the separation efficiency of photogenerated electron-hole pairs, but also construct Fenton reactions to convert *in-situ* formed inactive H_2O_2 into reactive radicals (such as $\cdot O_2{}^-$ and $\cdot OH$), which play significant roles in the oxidation of IPA. The effect of Fe(III) implantation in another porphyrinic MOF (PCN-222) on the visible light photocatalytic activity for the oxidation of IPA has been also studied. The same trend is observed, namely Fe@PCN-222 also shows enhanced activity for photocatalytic oxidation of IPA compared with bare PCN-222. This work provides a simple Fe(III) implantation strategy to improve the photocatalytic performance of MOFs based photocatalysts for organic compounds oxidation, and it is anticipated that the metal ions implantation strategy can also be applicable to other photocatalytic reactions, such as H_2 evolution and CO_2 reduction, by flexibly implanting specific metal ions in the MOFs structure.

Acknowledgments

Appendix A. Supplementary data

Supplementary data associated with this article can be found, in the online version, at http://dx.doi.org/10.1016/j.apcatb.2017.10.033.

References

[1] G. Zhang, G. Liu, L. Wang, J.T.S. Irvine, Chem. Soc. Rev. 45 (2016) 5951–5984.
[2] W.-J. Ong, L.-L. Tan, Y.H. Ng, S.-T. Yong, S.-P. Chai, Chem. Rev. 116 (2016) 7159–7329.
[3] M. Ge, Q. Li, C. Cao, J. Huang, S. Li, S. Zhang, Z. Chen, K. Zhang, S.S. Al-Deyab, Y. Lai, Adv. Sci. 4 (2017) 1600152.
[4] L. Shi, P. Li, W. Zhou, T. Wang, K. Chang, H. Zhang, T. Kako, G. Liu, J. Ye, Nano Energy 28 (2016) 158–163.
[5] T. Zhang, W. Lin, Chem. Soc. Rev. 43 (2014) 5982–5993.
[6] S. Wang, X. Wang, Small 11 (2015) 3097–3112.
[7] A. Dhakshinamoorthy, A.M. Asiri, H. García, Angew. Chem. Int. Ed. 55 (2016) 5414–5445.
[8] M. Wen, K. Mori, Y. Kuwahara, T. An, H. Yamashita, Appl. Catal. B: Environ. 218 (2017) 555–569.
[9] M. Wen, Y. Cui, Y. Kuwahara, K. Mori, H. Yamashita, ACS Appl. Mater. Interfaces 8 (2016) 21278–21284.
[10] M. Wen, K. Mori, Y. Kuwahara, H. Yamashita, ACS Energy Lett. 2 (2017) 1–7.
[11] L. Chi, Q. Xu, X. Liang, J. Wang, X. Su, Small 12 (2016) 1351–1358.
[12] T. Toyao, M. Saito, S. Dohshi, K. Mochizuki, M. Iwata, H. Higashimura, Y. Horiuchi, M. Matsuoka, Chem. Commun. 50 (2014) 6779–6781.
[13] W. Wang, X. Xu, W. Zhou, Z. Shao, Adv. Sci. 4 (2017) 1600371.
[14] C.-C. Wang, J.-R. Li, X.-L. Lv, Y.-Q. Zhang, G. Guo, Energy Environ. Sci. 7 (2014) 2831–2867.
[15] K.G.M. Laurier, F. Vermoortele, R. Ameloot, D.E.D. Vos, J. Hofkens, M.B.J. Roeffaers, J. Am. Chem. Soc. 135 (2013) 14488–14491.
[16] L. Shi, T. Wang, H. Zhang, K. Chang, X. Meng, H. Liu, J. Ye, Adv. Sci. 2 (2015) 1500006.
[17] R. Liang, L. Shen, F. Jing, W. Wu, N. Qin, R. Lin, L. Wu, Appl. Catal. B: Environ. 162 (2015) 245–251.
[18] R. Liang, F. Jing, L. Shen, N. Qin, L. Wu, J. Hazard. Mater. 287 (2015) 364–372.
[19] L. Shi, T. Wang, H. Zhang, K. Chang, J. Ye, Adv. Funct. Mater. 25 (2015) 5360–5367.
[20] D. Wang, R. Huang, W. Liu, D. Sun, Z. Li, ACS Catal. 4 (2014) 4254–4260.
[21] H. He, J.A. Perman, G. Zhu, S. Ma, Small 12 (2016) 6309–6324.
[22] H.-Q. Xu, J. Hu, D. Wang, Z. Li, Q. Zhang, Y. Luo, S.-H. Yu, H.-L. Jiang, J. Am. Chem. Soc. 137 (2015) 13440–13443.
[23] K.M. Choi, D. Kim, B. Rungtaweevoranit, C.A. Trickett, J.T.D. Barmanbek, A.S. Alshammari, P. Yang, O.M. Yaghi, J. Am. Chem. Soc. 139 (2017) 356–362.
[24] M.A. Nasalevich, M. van der Veen, F. Kapteijn, J. Gascon, CrystEngComm 16 (2014) 4919–4926.
[25] H. Zhang, G. Liu, L. Shi, H. Liu, T. Wang, J. Ye, Nano Energy 22 (2016) 149–168.
[26] D. Sun, Y. Fu, W. Liu, L. Ye, D. Wang, L. Yang, X. Fu, Z. Li, Chem. Eur. J. 19 (2013) 14279–14285.
[27] A.W. Peters, Z. Li, O.K. Farha, J.T. Hupp, ACS Appl. Mater. Interfaces 8 (2016) 20675–20681.
[28] Z. Sha, J. Wu, RSC Adv. 5 (2015) 39592–39600.
[29] S. Wang, X. Wang, Appl. Catal. B: Environ. 162 (2015) 494–500.
[30] R. Li, J. Hu, M. Deng, H. Wang, X. Wang, Y. Hu, H.-L. Jiang, J. Jiang, Q. Zhang, Y. Xie, Y. Xiong, Adv. Mater. 26 (2014) 4783–4788.
[31] M. Wen, K. Mori, T. Kamegawa, H. Yamashita, Chem. Commun. 50 (2014) 11645–11648.
[32] Y. Mi, H. Wen, Z. Wang, D. Cao, R. Xu, Y. Fang, Y. Zhou, Y. Lei, Nano Energy 30 (2016) 109–117.
[33] M. Liu, X. Qiu, M. Miyauchi, K. Hashimoto, J. Am. Chem. Soc. 135 (2013) 10064–10072.
[34] E. Brillas, I. Sires, M.A. Oturan, Chem. Rev. 109 (2009) 6570–6631.
[35] D. Yang, J. Feng, L. Jiang, X. Wu, L. Sheng, Y. Jiang, T. Wei, Z. Fan, Adv. Funct. Mater. 25 (2015) 7080–7087.
[36] Y. Su, Z. Wu, Y. Wu, J. Yu, L. Sun, C. Lin, J. Mater. Chem. A 3 (2015) 8537–8544.
[37] X. Geng, W. Li, F. Xiao, D. Wang, L. Yang, Catal. Sci. Technol. 7 (2017) 658–667.
[38] Y. Li, S. Ouyang, H. Xu, X. Wang, Y. Bi, Y. Zhang, J. Ye, J. Am. Chem. Soc. 138 (2016) 13289–13297.
[39] I.A. Menon, M.A.C. Beker, S.D. Persad, H.F. Haberman, Clin. Chim. Acta 186 (1990) 375–381.
[40] K. Komagoe, T. Katsu, Anal. Sci. 22 (2006) 255–258.
[41] B. Abeykoon, J.M. Grenèche, E. Jeanneau, D. Chernyshov, C. Goutaudier, A. Demessence, T. Devic, A. Fateeva, Dalton Trans. 46 (2017) 517–523.
[42] J.S. Anderson, A.T. Gallagher, J.A. Mason, T.D. Harris, J. Am. Chem. Soc. 136 (2014) 16489–16492.
[43] D. Feng, W.-C. Chung, Z. Wei, Z.-Y. Gu, H.-L. Jiang, Y.-P. Chen, D.J. Darensbourg, H.-C. Zhou, J. Am. Chem. Soc 135 (2013) 17105–17110.
[44] M. Jahan, Q. Bao, K.P. Loh, J. Am. Chem. Soc. 134 (2012) 6707–6713.
[45] B. Yao, C. Peng, W. Zhang, Q. Zhang, J. Niu, J. Zhao, Appl. Catal. B: Environ. 174–175 (2015) 77–84.
[46] L. Yang, J. Huang, L. Cao, L. Shi, Q. Yu, X. Kong, Y. Jie, Sci. Rep. 6 (2016) 27765.
[47] S. Ouyang, J. Ye, J. Am. Chem. Soc. 133 (2011) 7757–7763.
[48] H.-Y. Jiang, P. Li, G. Liu, J. Ye, J. Lin, J. Mater. Chem. A 3 (2015) 5119–5125.
[49] J. Guo, H. Zhou, S. Ouyang, T. Kako, J. Ye, Nanoscale 6 (2014) 7303–7311.
[50] H.-Y. Jiang, G. Liu, M. Li, J. Liu, W. Sun, J. Ye, J. Lin, Appl. Catal. B: Environ. 163 (2015) 267–276.
[51] H. Wang, T. Yu, X. Tan, H. Zhang, P. Li, H. Liu, L. Shi, X. Li, J. Ye, Ind. Eng. Chem. Res. 55 (2016) 8096–8103.
[52] S. Ouyang, P. Li, H. Xu, H. Tong, L. Liu, J. Ye, ACS Appl. Mater. Interfaces 6 (2014) 22726–22732.
[53] L. Shi, K. Chang, H. Zhang, X. Hai, L. Yang, T. Wang, J. Ye, Small 12 (2016) 4431–4439.
[54] X. Meng, Q. Yu, G. Liu, L. Shi, G. Zhao, H. Liu, P. Li, K. Chang, T. Kako, J. Ye, Nano Energy 34 (2017) 524–532.
[55] L. Huang, J. Yang, X. Wang, J. Han, H. Han, C. Li, Phys. Chem. Chem. Phys. 15 (2013) 553–560.
[56] S. Naya, T. Niwa, T. Kume, H. Tada, Angew. Chem. Int. Ed. 53 (2014) 7305–7309.
[57] J. Sun, X. Li, Q. Zhao, M.O. Tadé, S. Liu, J. Mater. Chem. A 3 (2015) 21655–21663.
[58] G. Liu, P. Niu, L. Yin, H.-M. Cheng, J. Am Chem. Soc. 134 (2012) 9070–9073.
[59] H. Katsumata, M. Taniguchi, S. Kaneco, T. Suzuki, Catal. Commun. 34 (2013) 30–34.